IMPLANTABLE DEVICES FOR BONE REGENERATION: GENERATING FLUID FLOW INDEPENDENT OF COMPRESSION TO PROMOTE BONE GROWTH

by

SOPHIA GUITTEAU

A THESIS

Presented to the Department of Human Physiology
and the Robert D. Clark Honors College
in partial fulfillment of the requirements for the degree of
Bachelor of Science

May, 2024

An Abstract of the Thesis of

Sophia Guitteau for the degree of Bachelor of Science
in the Department of Human Physiology to be taken May, 2024

Title: Implantable Devices for Bone Regeneration: Generating Fluid Flow Independent of Compression to Promote Bone Growth

Approved: *Keat Ghee Ong, Ph.D.*
Primary Thesis Advisor

All cells display the incredible ability to detect external stimuli, such as mechanical stress, and convert those stimuli into biochemical signals and subsequent cellular responses. In bones, a type of bone cell called osteocytes are the main conductors of this mechanotransduction. Osteocytes reside in spaces called lacunae and are connected by channels called canaliculi. Gravitational pull, bearing weight, and muscle contraction all cause small deformations of our bones and thus cause interstitial fluid movement through the lacunar-canalicular network. Osteocytes, which are connected by cytoplasmic processes, communicate these mechanical stresses and translate them into cellular mechanisms that augment the bone mass in the area of the stress.

Typical therapies for bone fractures include stabilization and mechanical loading. However, in instances where fractures are severe and a significant section of bone is lost, this mechanical loading is not a feasible therapy. Therefore, in the Ong Lab, we are looking at ways to directly induce this fluid shear stress at a gap fracture site to study the role of fluid flow in bone regeneration and enhance the rate of bone healing in instances of severe fractures. There are numerous ways to induce fluid shear stress, but our research uses magnetohydrodynamics. This method involves combining a magnetic field with a perpendicular electrical field from cathode and anode electrodes powered by a power supply. The combination of these fields generates a force that acts on charged particles, driving them in a direction perpendicular to both the electric and magnetic fields.

Previous benchtop and *in vitro* experiments have demonstrated that the device successfully induces fluid flow. Moreover, the magnitude of the force on the conductive fluid can be altered by changing the electrical or magnetic field strength. We have also conducted three *in vivo* pilot studies in Wistar rats, which have generally produced data in support of the hypothesis that the device induces fluid movement in the fracture site and enhances bone growth in that area. The device and technology thus may offer applications in the clinical sphere as a novel therapy for bone regeneration.

Acknowledgments

I am incredibly grateful to my wide network of support both personal and professional that helped me over the past few years. Your contributions were invaluable to the completion of this thesis and my growth as a student and person.

Thank you to Dr. Ong and Eyerusalem Gebreyesus for welcoming me into the lab at Knight Campus and guiding me through my first experience in research. Thank you to Dr. Munger for being an impactful teacher early in my Clark Honors College experience and advisor on this project.

Thank you to my friends who encouraged me through the long hours spent on this project and for listening to every rendition of my various presentations on this work.

Thank you to my fellow undergraduate lab researchers whose own tenacity and desire for knowledge inspired mine.

Lastly, thank you to my parents and brother for listening to every success and frustration along the way. Most of all, thank you for always encouraging my curiosity and for teaching me to never stop learning.

Table of Contents

List of Figures

List of Tables

Introduction

In the 19th century, German surgeon Julius Wolff was the first to develop a law describing the remarkable process that is bone remodeling. Wolff postulated that when bone endures mechanical loading above a certain threshold it will reinforce itself with bone growth in that area, and mechanical loading below a certain threshold will result in bone resorption (Rowe, 2023; Mavčič & Antolič, 2012). At the basis of this physiological phenomenon is the concept of mechanotransduction, where mechanical signals to cells are translated into a variety of secondary actions, including cell proliferation and differentiation (Stewart, 2020). The main conductors of bone mechanotransduction are osteocytes. These mature bone cells, representing terminal differentiation of bone cells, are the most abundant and long-lived cell type in bone, comprising 95% of bone cells. They regulate the processes of bone remodeling by modulating the activity of osteoblasts, bone builders, and osteoclasts, bone resorbers (Qin et al., 2020).

Bone is made up of two types of bone tissue: spongy and compact, which describe the density of the porous structure (Cooper, 2016). In the outer compact cortical bone, osteocytes are housed within spaces called lacunae, which are connected via canaliculi. Together, these spaces form the lacuno-canalicular network (Cardoso, 2013). Osteocytes are linked via their processes through the canaliculi, allowing for communication between cells. Therefore, when mechanical load causes interstitial fluid to flow through the lacuno-canalicular network, the osteocytes detect this stress and communicate with other osteocytes to elicit a secondary action (Stewart, 2020). This fluid shear stress (FSS) is the main mechanical stimulus to osteocytes (Qin et al., 2020; Cardoso, 2013). Mechanosensors on the membranes of these cells detect this movement of fluid (Stewart, 2020). Harnessing this natural physiological occurrence of fluid movement driving bone generation could therefore be key to novel fracture therapy.

Types of fractures where there is a critical-sized defect and concern of non-union are where this physiologic process is especially useful. A critical-sized defect is a type of bone defect that will not heal spontaneously and thus results in non-union (Roddy, 2018). Every year in the United States, about 100,000 cases of fractures result in non-union. These injuries are associated with significant financial costs, psychological and physical burden, and extended healing time (Huang, 2022; Mavčič & Antolič, 2012). Standard treatment involves stabilization and bone grafting, either used independently or together (Huang, 2022; Tsimbouri et al., 2017), while less standard care options include scaffolds and stem cell therapy (Huang, 2022). Moreover, the treatment procedure for fractures and osteotomies is poorly defined. While load bearing is recommended to induce mechanical strain in the fracture area, it is difficult to regulate this strain (Mavčič & Antolič, 2012). A study in rats where researchers replicated critical-size gap injuries showed that too much load too fast is associated with poor vascular regrowth and reduced bone formation (Boerckel et al., 2011), however rigid fixation prolongs healing time because the fracture site is over-protected from mechanical stimulation (Mavčič and Antolič, 2012).

Currently, there are experimental methods that try to generate a form of mechanical stimulus to induce bone growth, including whole-body vibrations (Marin-Cascales et al., 2018) and nano vibrations (Tsimbouri et al., 2017), shockwaves (Wang FS), electrical stimulation (Griffin & Bayat, 2011), and low-intensity pulsed ultrasound. Some of these methods have been reported as successful in enhancing bone mass density or accelerating healing, but generally, the efficacy of these treatments remains controversial and needs further investigation (Stewart et al., 2020).

The method that this study investigates relies on magnetohydrodynamics (MHD). In MHD, a power source, an anode, and a cathode generate an electric current through an electrically conductive fluid. A magnetic field is then directed perpendicular to this current. Together, these fields create a force that directs fluid flow perpendicular to both the electrical and magnetic fields. Benefits of this system include simple fabrication on a small scale and high efficiency (Al-Habahbeh, 2016). The specific force that acts on the electrically conductive fluid is called Lorentz force and can be expressed mathematically as:

$$F = \sigma E \times B$$

E represents the induced electric current density (V/m), B represents the magnetic flux density (T), and σ is the conductivity of the fluid (S/m). The conductivity of interstitial fluid is estimated at 2.0 S/m (Stinstra et al., 2005).

In 2023, the Knight Campus, a research department located at the University of Oregon, produced a study suggesting that a device that utilizes magnetohydrodynamics promotes fibroblast cell migration *in vitro*. The researchers determined that the device should generate a flow rate of 7μm/s, based on existing biomechanical regulatory models that suggest this fluid flow is conducive to bone regeneration. Moreover, a current of 1mA and a magnetic field of 0.1mT would be sufficient to generate 7μm/s (Gebreyesus, 2023). The following study therefore presents the adaptation of this MHD pump into an implantable device for the investigation of inducing FSS through a femoral fracture and the results of three pilot studies using this device.

Methods

Mechanical Testing of Bone Plate

Because this study aims to test the efficacy of the device in generating fluid flow independent of compression, a bone plate was required to resist compression in the femurs of the Wistar rat subjects. Bone plates of various materials were connected to a mechanical tester for axial stiffness testing: polysulfone (PSU), polyether ether ketone (PEEK), and ultra-high molecular weight polyethylene (UHMWPE). Negative axial force (compression) was added to the plates by the machine, and the subsequent displacement was measured. This testing was necessary in determining the stiffest material. An additional test was run on PEEK, to assess stiffness with the sleeve attachment screwed in.

Device Fabrication

Mold for sleeves

To create the sleeves, see Figure 2 for reference, silicone molds were used to ensure proper encapsulation of the electrodes and silver epoxy. First, sleeves for the silicone mold were 3-D printed with Formlabs clear resin. Once printed, they were washed in 90% isopropyl alcohol and UV-cured with the respective washing and curing times determined by Formlabs. Outer shells to hold the silicone were 3-D printed with plastic filament, then secured onto a plastic platform with Dymax light-cured adhesive. The 3-D printed sleeves were arranged on the plastic platform within the outer shell, ensuring that the side of the sleeves with the projection for the silicone tube faced upward. Equal parts of the silicone part a and part b were mixed until homogenous and then vacuumed to remove air bubbles from the mixture. The liquid silicone was then poured over the sleeves until the projections were covered. These molds were left in the

refrigerator for one hour to remove any remaining bubbles, then left at room temperature overnight to cure. After ~24 hours, the molds were set and placed in an oven at 37℃ for two hours to ensure that they were fully cured. Once fully set, the 3-D printed sleeves were removed leaving behind the molds for the final sleeves.

Electrode pairs

The electrodes for the sleeves were made from 0.5 mm thick glass sheets. These sheets were cut into rectangles with the dimensions 7.3 mm x 4.7 mm. To make these glass pieces conductive electrodes, they were etched and coated with a 10nm layer of titanium followed by a 200nm layer of platinum. To connect the electrodes to the circuit board, 28cm long pieces of 0.001" thick stainless-steel wire were used. A piece of 2mm long 0.5 mm x 0.3 mm thick micro brass tubing was threaded and clamped on each end of exposed stainless-steel wire. The stainless-steel wires were folded in half and taped to a piece of foil so that the two ends were arranged next to one another. One electrode was designated per end of each piece of wire, and the conductive faces were faced upward. Equal parts of MG Chemical silver conductive epoxy adhesive were mixed until homogenous, and a thin line of epoxy was applied to each electrode. The ends of the stainless-steel wires with the micro brass segments were then secured onto the epoxy, and these electrode pairs were cured in an oven at 90℃ for 10 minutes.

Electrode sleeves

To create the final sleeves, a hole was created at each projection point in the mold where the wires would leave out of the sleeve. An electrode pair was then threaded through each of these holes through the backside of the mold. The conductive faces of each electrode were taped to protect these faces from the Masterbond. These taped sides were superglued to either side of the center wall of the sleeve molds, ensuring that the wires traveled toward the projection end of the mold. The wires were pulled until there was just enough slack for them to rest at the base of

the mold and splay around the space where a screw would go for securing the sleeve to the bone plate. The wires, still connected into a continuous wire, were then threaded through a 13cm silicone tube. About 1mm of these silicone tubes were then pulled into the mold so that the Masterbond would encase the tubing. Parts a and b of the Masterbond were mixed in a 4:1 ratio until homogenous. Using a syringe and syringe tip, the silicone mold was filled with Masterbond, and the sleeves were vacuumed to remove any excess air bubbles. These were cured at 90℃ for 30 minutes then left out overnight to fully cure.

Circuit boards

The circuit boards were fabricated by soldering the required components onto the printed circuit boards (PCBs). A soldering paste was used to attach each component to its respective spot on the PCB. These pieces were then heated in an oven with a setting that reached 255°C before cooling down. This solidified the pieces onto the PCB. The microcontroller component was then programmed with Arduino. A second PCB with the ground pad for the battery was then soldered onto the first PCB. To this board, a battery holder was soldered on.

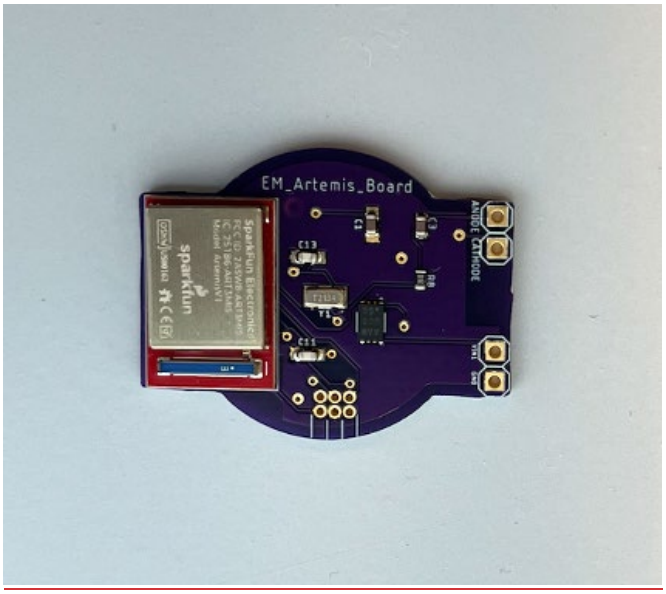

Figure 1: Circuit Board

The PCB is assembled with components. On the left is the microcontroller element of the board.

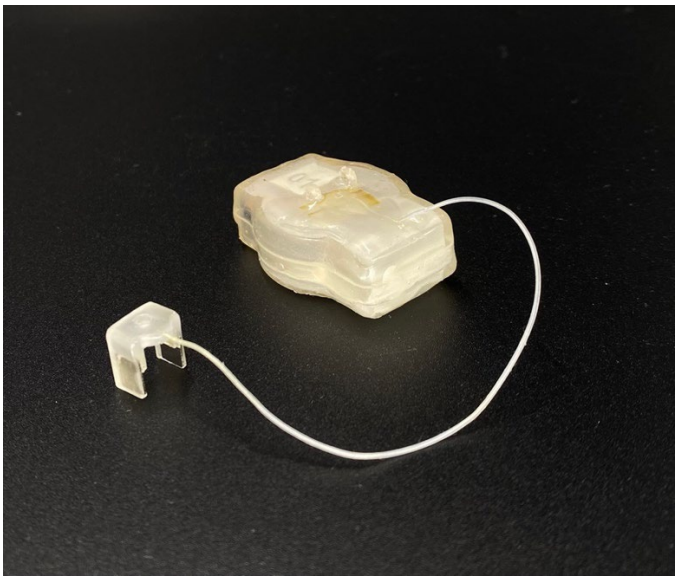

Figure 2: Complete Device

The assembled device including the power unit on the right-hand side connected via silicone tube-encased wires to the electrodes housed in the molded sleeve.

Surgery

All animal procedures were approved by the University of Oregon Institutional Animal Care and Use Committee (IACUC protocol AUP-20-25). The procedure was based on previously published work (Klosterhoff et al., 2017). The animals were housed with unlimited access to food and water and acclimatized to a 12:12 h light:dark cycle before experimental use. Under isoflurane anesthesia (1.5-2.5%), a bone plate was fixated on the femur to ensure stabilization during the defect portion of the surgery. A unilateral 2 mm segmental defect was surgically made in the mid-diaphysis of the femur using an oscillating saw. The sleeve with the electrodes was fed through a keyhole incision in the abdominal wall to the defect region. This sleeve was screwed down onto the bone plate so that it surrounded either side of the defect. The power component was then implanted in the abdomen and secured to the abdominal wall. The peritoneum and musculature at each of the incision sites were sutured and the skin was closed with wound clips. All subjects received a subcutaneous injection of sustained-release buprenorphine for analgesia.

In Vivo Treatment

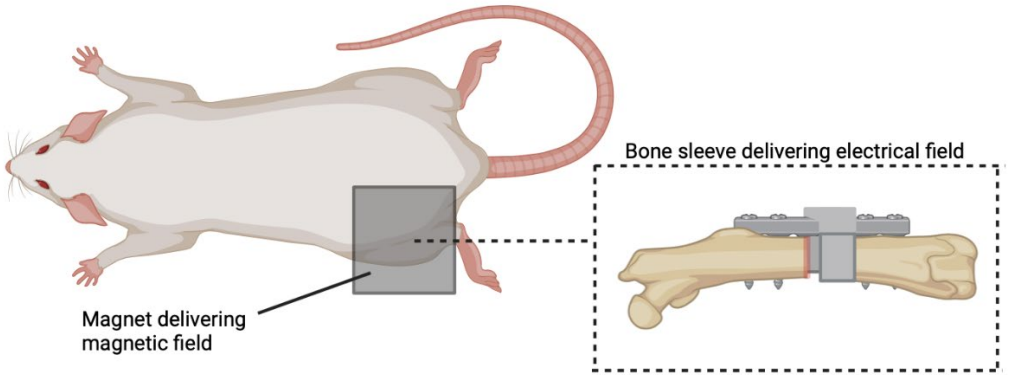

Figure 3: Treatment Illustration

Illustration of the treatment set-up. The rats were placed in a prone position. Their left leg was extended into the space between the two magnets and taped down for security. The rats received constant sedation from a nose cone throughout treatment.

Pilot I

6 Wistar rats (3 control and 3 experimental) underwent the femoral defect surgery. Treatment was started on the third postoperative day for the rat subjects. The experimental group received concurrent 20 minutes of electrical field induction and 20 minutes of magnetic field over the leg, to induce fluid flow. The control group received the same 20 minutes of electrical field induction and 20 minutes of magnetic field but separately, thus not inducing fluid flow. The treatment schedule involved two days of treatment followed by one day of rest with no treatment. Aimed for 8 weeks.

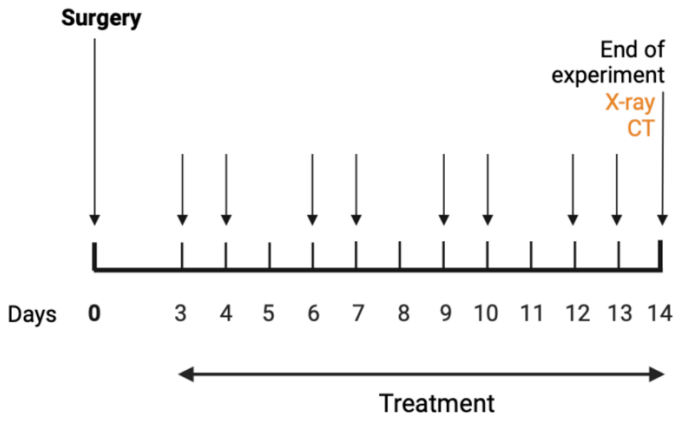

Figure 4: Pilot I Treatment Schedule Schematic

Pilot II

5 Wistar rats (2 control and 3 experimental) underwent the femoral defect surgery. Treatment was started on the seventh postoperative day for the rat subjects. The experimental and control groups received the same treatment types as outlined in Pilot I. However, the treatment schedule for Study 2 involved one day of treatment followed by two days of rest to minimize excessive disruption and provide a recovery period. Aimed for 4 weeks.

In Pilot III

6 Wistar rats (3 control and 3 experimental) underwent femoral defect surgery. Treatment was started on the seventh postoperative day for the rat subjects. The experimental and control groups received the same treatment types as outlined in Study 1. The treatment schedule involved one day of treatment followed by two days of rest. Aimed for 8 weeks.

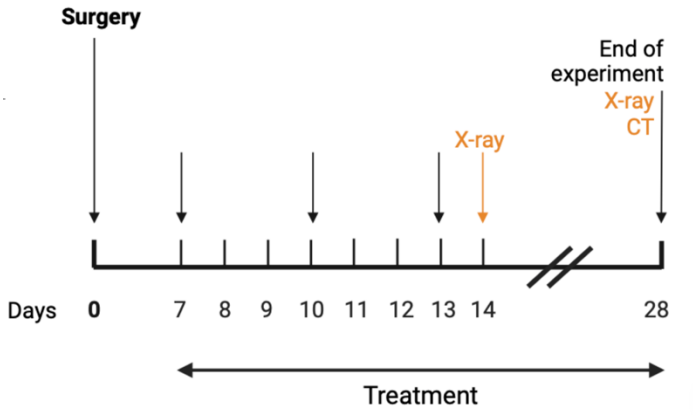

Figure 5: Pilots II and III Treatment Schedule Schematic

Radiological Evaluation

To evaluate the bone healing, Faxitron® x-ray images were taken at 2- and 4 weeks post-surgery. These images were used to assess the placement of the bone plate during surgery, confirm that all parts of the device remained intact, and qualitatively assess the state of bone healing. Additionally, at the endpoint of each pilot study, the animals were euthanized using CO2 asphyxiation. The femurs were dissected from the soft tissue and imaged using microCT to quantify bone volume and generate a 3-D model of the defect site for evaluating bone regrowth density. All femur samples were placed in 10% normal buffered formalin for future histological evaluation.

Results

Mechanical Testing

The mechanical testing demonstrated that the bone plates fabricated with PEEK were the stiffest, with an axial stiffness of 74.45 (SD = ± 4.13) N/mm. The polysulfone plate had a stiffness of 51.73 (SD = ± 1.08) N/mm and the UHMWPE had 44.23 (SD = ± 9.24) N/mm. An additional test on the PEEK with the sleeve screwed in demonstrated an increased stiffness of 93.50 (SD = ± 1.42) N/mm.

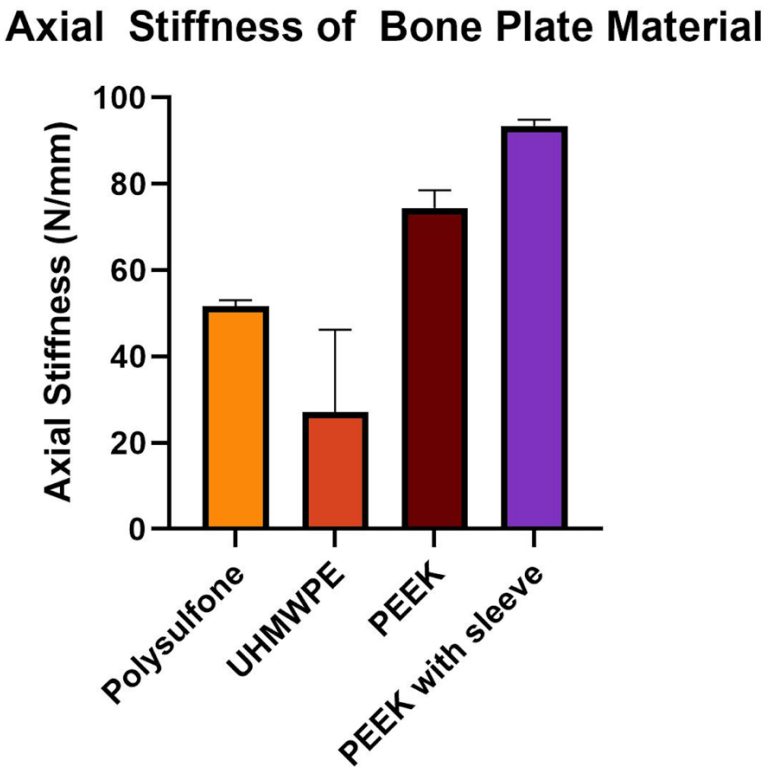

Figure 6: Mechanical Testing of Bone Plates

Comparison of axial stiffness values of bone plates made from different materials: polysulfone, UHMWPE, PEEK, and PEEK without sleeve.

In Vivo Treatments

Pilot I – Two weeks

From Pilot I, the data demonstrated a trend opposite to the expected results. The flow group had an average bone mass at the defect area of 0.316 (SD = $\pm$0.22) mm^3, while the no-flow group demonstrated an average bone mass of 1.06 (SD = $\pm$0.13) mm^3 in the defect area. Statistical analysis could not be run on this pilot alone due to a limited data set.

Flow Group	No-Flow Group
0.572 mm^3	1.02 mm^3
0.171 mm^3	1.21 mm^3
0.204 mm^3	0.951 mm^3

Table 1: Pilot I Bone Regrowth Volume

Bone volume in the defect area was measured using microCT to quantify the regrowth of bone after two weeks of treatment. The treatment (flow) group demonstrated an average increase of 0.316 (SD = $\pm$ 0.22) mm^3, while the no-flow group demonstrated an average increase of 1.06 (SD = $\pm$ 0.13) mm^3.

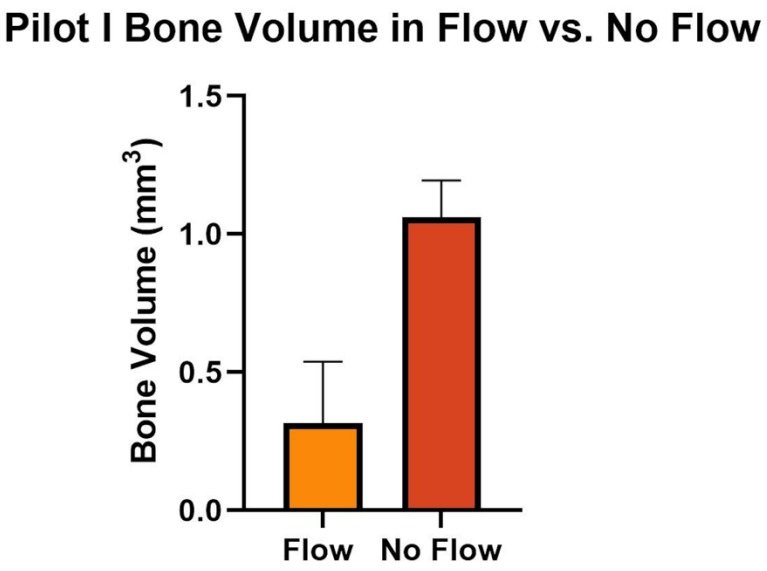

Figure 7: Graphical Representation of Pilot I Bone Regrowth Volume

Pilot II – Four weeks

In pilot II, the data demonstrated a trend that aligned with the expected results. The flow group had an average bone mass increase at the defect site of 6.65 (SD = $\pm$ 6.43) mm^3, while the no-flow group showed an increase of 1.29 (SD = $\pm$ 0.78) mm^3. Statistical analysis could not be run on this data set due to limited data.

Flow Group	No-Flow Group
14.00 mm^3	1.84 mm^3
2.02 mm^3	0.73 mm^3
3.93 mm^3	

Table 2: Pilot II Bone Regrowth Volume

Bone volume in the defect area was measured using microCT to quantify the regrowth of bone after two weeks of treatment. The treatment (flow) group demonstrated an average increase of 6.65 (SD = $\pm$ 6.44) mm^3, while the no-flow group demonstrated an average increase of 1.29 (SD = $\pm$ 0.78) mm^3.

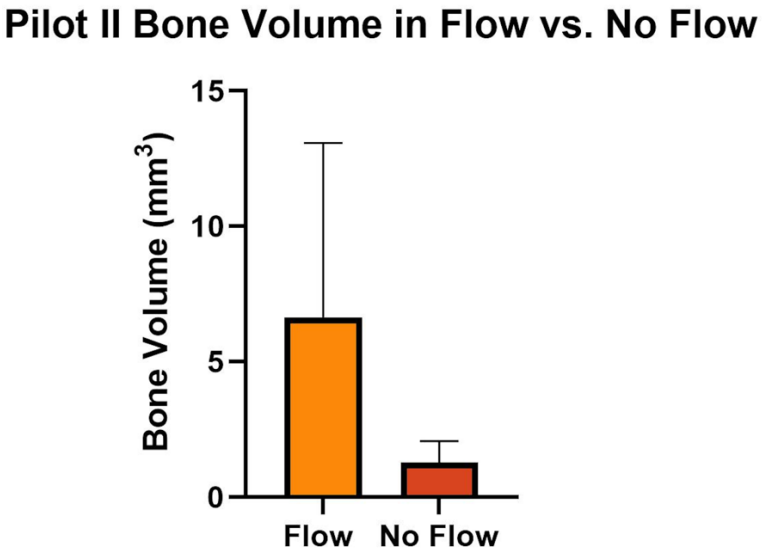

Figure 8: Graphical Representation of Pilot II Bone Regrowth Volume.

Pilot III – Four Weeks

In Pilot III, the data demonstrated a trend that aligned with the expected results. The flow group demonstrated an average increase in bone mass at the defect site of 4.21 (SD = $\pm$ 4.89) mm^3. The no-flow group demonstrated an average increase in bone mass at the defect site of 2.45 (SD = $\pm$ 2.75) mm^3. Statistical analysis could not be run on this data set due to limited data.

Flow Group	No-Flow Group
9.8 mm^3	0.55 mm^3
1.3 mm^3	1.2 mm^3
1.47 mm^3	5.6 mm^3

Table 3: Pilot III Bone Regrowth Volume

Bone volume in the defect area was measured using microCT to quantify the regrowth of bone after two weeks of treatment. The treatment (flow) group demonstrated an average increase of 4.21 (SD = $\pm$ 4.89) mm^3, while the no-flow group demonstrated an average increase of 2.45 (SD = $\pm$ 2.75) mm^3.

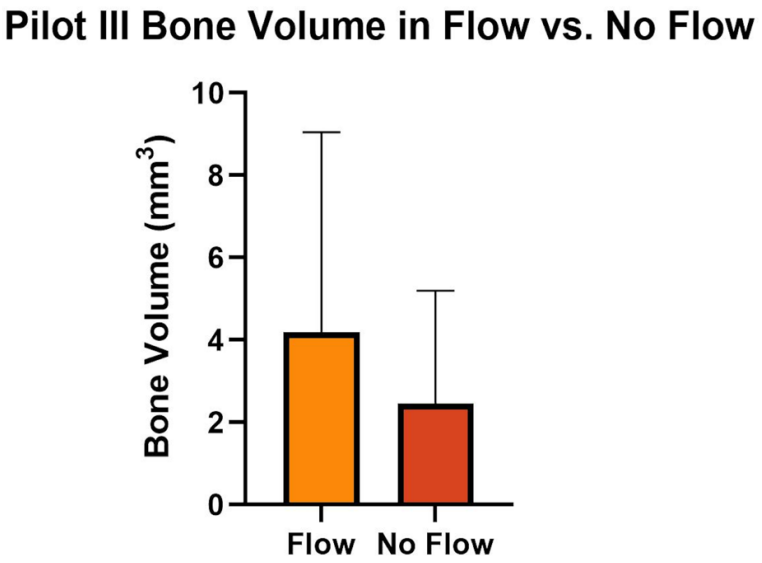

Figure 9: Graphical Representation of Pilot III Bone Regrowth Volume.

Combined Data Sets of Pilot II and Pilot III

Because Pilots II and III lasted the same duration, four weeks, and the protocols remained the same for both, the two data sets could be combined to run statistical analyses. A Mann-Whitney U test was run with Prism, and no statistical significance could be determined.

Discussion

Transitioning a device from *in vitro* to *in vivo* experiments inevitably presents a host of challenges that require modifications in the fabrication of the device. This is because a live subject provides a dynamic physiologic environment that is also physically moving, thus disrupting the device chemically and physically. During each pilot study, these challenges presented themselves, and aspects of the device were reworked for the next pilot study.

In March of 2021, Eyerusalem Gebreyesus began working on this project, and with the help of undergraduate Alice Park, developed a working model of this device *in vitro*. Efforts were then made to transition the *in vitro* model to an *in vivo* device. When I joined the Ong lab, in October of 2022, nearly all components of the device's fabrication were different than they are today.

In October 2022, the sleeves were 3-D printed with biocompatible resin, and the electrodes were adhered to the sleeves with Dymax adhesive. This process was time-consuming and flawed, and it was difficult to completely enclose the silver epoxy used to adhere the wires to the electrodes. A multimeter was used to check for exposed silver, and it took many layers of Dymax to eliminate continuity. In January 2023, I began to design new sleeves with deeper spaces for the electrodes and small hooks that would hold the wires in place while adhering. I also designed three new sleeves to test various sizes to fit around the bone plate. We hoped to minimize the size of the device, but the amount of Dymax that was required hindered this goal. To minimize the time spent on fabricating the devices, we switched to creating silicone molds in which we created the final sleeves. The discontinuation of the Dymax in this process also meant the sleeves could be made much smaller and consistently fit over the bone plate. This resolved the issue of exposed silver and maneuvering the wires into place. A pilot study conducted before

I joined the lab also showed that fluid was entering the power supply when implanted, so efforts were made to better seal this power supply.

In April 2023, I participated in my first pilot study. This study ended prematurely because the devices stopped transmitting. Gebreyesus worked to troubleshoot the supposed circuit board issues and determined that the Bluetooth interval programmed into the device was too frequent. We conducted a study to test the battery duration on different Bluetooth intervals, and a new Bluetooth interval was programmed onto the device and the power consumption was reduced to 80uA when the device was idle. Since Pilot I showed that fluid was still entering the devices, we switched over to Dymax adhesive for coating the entire enclosure. In June of 2023, I explored ways to reduce strain on the silicone tube that insulated the wires, because this component is fragile inside the rat subjects. I began using a new method for enclosing the tube in the sleeve.

In July 2023, we conducted Pilot II and tested the new enclosure sealing, fabrication techniques, and Bluetooth interval. Again, the devices had prematurely stopped transmitting, and we found that a few electrodes had eroded. However, since the devices lasted for four weeks *in vivo,* we collected data that demonstrated the longer-term effects of this device, and the data supported the hypothesis.

In March of 2023, we conducted Pilot III. We were hoping to corroborate data from Pilot II and reach an ideal 8-week long study. The device again failed prematurely at four weeks. The takedown of the rats showed that a few of the tubes had broken at the junction between the tube and the sleeve, due to a difference in mechanical properties of the tube and the sleeve. Analysis of the devices showed that three of the batteries had been drained for an undetermined reason.

Currently, fabrication challenges include the breaking of the tube at the junction and the eroding electrodes, and we need to determine why the batteries drained, we suspect a short somewhere in the power supply.

Over the course of my time at the lab, we also made alterations to the treatment schedule. In Pilot I, the treatment schedule was two days of treatment followed by one rest day, and this began on the third postoperative day. Qualitative analysis of the rat subjects' aggressive temperament during this treatment schedule demonstrated that this was potentially too soon to begin treatment and too rigorous of a treatment schedule. Additionally, as shown in Table 1, the data reflected an opposite trend to what we expected. The no-flow group had more bone density in the defect area than the flow group by the end of the study. We hypothesized that beginning the flow that soon postoperatively and inducing flow too often was disrupting the healing process. Therefore, in Pilots II and III, the treatment began on the seventh postoperative day and the treatment schedule was one day of treatment followed by two days of rest. As demonstrated in Table 2 and Table 3, the data overall validated our expectations. This suggests that maximizing healing relies on a balance between rest and stimulating fluid flow.

The electrodes were tested for degradation after the most recent pilot study in cell culture media, a fluid that mimics interstitial fluid in its composition of ions, nutrients, hormones, and other biomarkers. In this short study, the electrodes showed no signs of degradation despite maintaining the electrical field for 6 hours (equivalent to 18 treatments). This result suggests the degradation is related to either physical movement of the rat subject wearing down the electrodes, or some other physiological condition, such as changes in tissue pH postoperatively due to chronic inflammation. A study on tissue pH changes in response to plantar tissue and gastrocnemius muscle incision found that pH was decreased up to four days after the plantar

tissue incisions and up to seven days for the gastrocnemius incision. The data from the gastrocnemius incision showed significance (Woo, 2004). The femoral defect surgery used in this study involves deep incisions into several upper leg muscles and the abdominal wall, therefore it would be reasonable to assume that the surrounding tissue experiences some pH drop for at least the first postoperative week. While platinum, the deposited material for the electrodes, is generally highly resistant to pH changes and oxidation, there is some evidence that dissolution can occur under certain conditions such as fuel cells (Topalov, 2014). Current efforts made to mitigate the degradation of these electrodes include fabricating electrodes with a thicker layer of platinum.

Another current fabrication challenge has been the device breaking at the junction of the silicone tubing and the sleeve. This is likely due to a mismatch in mechanical properties: the sleeve is very stiff, and the tube is very pliable. Typical cables include a "cable strain relief" component that merges the two materials. I have been testing different methods of replicating a cable strain relief component, however, challenges arise with ensuring biocompatibility and that all the materials adhere together.

Existing literature supports the notion that healing is dependent on a combination of immobilization and compression. However, the postoperative period is not guided by strict instructions on duration of rest or amount of load bearing (Mavčič & Antolič, 2012). Therefore, this study, in part, aims to investigate the ideal treatment timeline. This study also aims to investigate different schedules of inducing more or less fluid shear stress. For example, existing literature discusses the practice of "dynamization" versus "reverse dynamization". Dynamization describes increasing interfragmentary movement (IFM), typically by changing the fixation from stable to flexible. Reverse dynamization would be decreasing IFM. However, the literature on

animal studies investigating dynamization is inconsistent (Glatt, 2017). In the context of an MHD device, dynamization would look like increasing either the electrical field or magnetic field flux, or both, to increase the amount of fluid shear stress. Reverse dynamization would look like decreasing one or both of those variables to decrease fluid shear stress. It is thought that different amounts of stress are conducive to different stages of bone healing e.g. fibrous tissue is promoted in areas of moderate to high tensile strain and bone formation occurs in areas of low to moderate tensile strain (Glatt, 2017). Therefore, reverse dynamization may best replicate the natural shift toward less strain as the fracture heals and promote the best healing.

To fully support the efficacy of this device, additional future studies must be conducted for further data collection and evidence of statistical significance between the no-flow and flow groups. Overall, this device shows promising applicability for inducing bone growth over gap fractures while a patient remains immobilized, or in individuals such as the elderly or those who have sustained multiple injuries and need to delay rehabilitation. This will mitigate the need for early compression on the bone which may ultimately disrupt the healing process.

Bibliography

Al-Habahbeh, O., et al., (2016). Review of magnetohydrodynamic pump applications. *Alexandria Engineering Journal*, 55(2): p. 1347-1358.

Boerckel, J. D., Uhrig, B. A., Willett, N. J., Huebsch, N., & Guldberg, R. E. (2011). Mechanical regulation of vascular growth and tissue regeneration in vivo. *Proceedings of the National Academy of Sciences of the United States of America*, 108(37), E674–E680.

Cardoso, L., Fritton, S. P., Gailani, G., Benalla, M., & Cowin, S. C. (2013). Advances in assessment of bone porosity, permeability and interstitial fluid flow. *Journal of biomechanics, 46(2), 253–265.*

Cooper, D.M.L., Kawalilak, C.E., Harrison, K. et al. (2016). Cortical Bone Porosity: What Is It, Why Is It Important, and How Can We Detect It?. *Current Osteoporosis Report,s* 14, 187–198

Ekegren, C. L., Edwards, E. R., de Steiger, R., & Gabbe, B. J. (2018). Incidence, Costs and Predictors of Non-Union, Delayed Union and Mal-Union Following Long Bone Fracture. *International journal of environmental research and public health*, 15(12), 2845.

Gebreyesus, E. A., Park, A., Guldberg, R. E., & Ong, K. G. (2023). In vitro magnetohydrodynamics system for modulating cell migration. *Biomedical physics & engineering express*, 9(2)

Glatt, V., Evans, C. H., & Tetsworth, K. (2017). A Concert between Biology and Biomechanics: The Influence of the Mechanical Environment on Bone Healing. *Frontiers in physiology*, 7, 678.

Griffin, M., & Bayat, A. (2011). Electrical stimulation in bone healing: critical analysis by evaluating levels of evidence. *Eplasty*, 11, e34.

Huang, E. E., Zhang, N., Shen, H., Li, X., Maruyama, M., Utsunomiya, T., Gao, Q., Guzman, R. A., & Goodman, S. B. (2022). Novel Techniques and Future Perspective for Investigating Critical-Size Bone Defects. *Bioengineering (Basel, Switzerland)*, 9(4), 171.

Klosterhoff, B. S., Ghee Ong, K., Krishnan, L., Hetzendorfer, K. M., Chang, Y. H., Allen, M. G., Guldberg, R. E., & Willett, N. J. (2017). Wireless Implantable Sensor for Noninvasive, Longitudinal Quantification of Axial Strain Across Rodent Long Bone Defects. Journal of biomechanical engineering, 139(11), 1110041–1110048. https://doi.org/10.1115/1.4037937

Marín-Cascales, E., Alcaraz, P. E., Ramos-Campo, D. J., Martinez-Rodriguez, A., Chung, L. H., & Rubio-Arias, J. Á. (2018). Whole-body vibration training and bone health in postmenopausal women: A systematic review and meta-analysis. *Medicine*, 97(34)

Mavčič, B., & Antolič, V. (2012). Optimal mechanical environment of the healing bone fracture/osteotomy. *International orthopaedics*, 36(4), 689–695.

Qin, L., Liu, W., Cao, H. et al. (2020). Molecular mechanosensors in osteocytes. *Bone Res*, 8, 23.

Roddy, E., DeBaun, M. R., Daoud-Gray, A., Yang, Y. P., & Gardner, M. J. (2018). Treatment of critical-sized bone defects: clinical and tissue engineering perspectives. *European journal of orthopaedic surgery & traumatology : orthopedie traumatologie*, 28(3), 351–362.

Rowe P, Koller A, Sharma S. (2023). Physiology, Bone Remodeling. *In: StatPearls [Internet]*.

Stewart, S., Darwood, A., Masouros, S., Higgins, C., & Ramasamy, A. (2020). Mechanotransduction in osteogenesis. *Bone & joint research*, 9(1), 1–14.

Stinstra, J. G., Shome, S., Hopenfeld, B., & MacLeod, R. S. (2005). Modelling passive cardiac conductivity during ischaemia. Medical & biological engineering & computing, 43(6), 776–782.

Topalov, Angel A., Serhiy Cherevko, Aleksandar R. Zeradjanin, Josef C. Meier, Ioannis Katsounaros, and Karl J. J. Mayrhofer. (2014). Towards a Comprehensive Understanding of Platinum Dissolution in Acidic Media. *Chem. Sci. 5, no. 2*, 631–38.

Tsimbouri, P. M., Childs, P. G., Pemberton, G. D., Yang, J., Jayawarna, V., Orapiriyakul, W., Burgess, K., González-García, C., Blackburn, G., Thomas, D., Vallejo-Giraldo, C., Biggs, M. J. P., Curtis, A. S. G., Salmerón-Sánchez, M., Reid, S., & Dalby, M. J. (2017). Stimulation of 3D osteogenesis by mesenchymal stem cells using a nanovibrational bioreactor. *Nature biomedical engineering*, 1(9), 758–770.

Young Cheol Woo, Soo Seog Park, Alberto R. Subieta, Timothy J. Brennan. (2004). Changes in Tissue pH and Temperature after Incision Indicate Acidosis May Contribute to Postoperative Pain. *Anesthesiology*,101:468–475.